

# Extending acoustic in-line pipe rheometry and friction factor modeling to low-Reynolds-number, non-Newtonian slurries

Hugh P. Rice<sup>1,2</sup>  | Jamie L. Pilgrim<sup>1,3</sup> | Michael Fairweather<sup>1</sup> | Jeff Peakall<sup>4</sup> | David Harbottle<sup>1</sup> | Timothy N. Hunter<sup>1</sup>

<sup>1</sup>School of Chemical and Process Engineering, University of Leeds, Leeds, UK

<sup>2</sup>School of Mechanical Engineering, University of Leeds, Leeds, UK

<sup>3</sup>Sellafield Ltd, Hinton House, Birchwood Park Avenue, Warrington, UK

<sup>4</sup>School of Earth and Environment, University of Leeds, Leeds, UK

## Correspondence

Hugh P. Rice, School of Chemical and Process Engineering, University of Leeds, Leeds LS2 9JT, UK.

Email: h.p.rice@leeds.ac.uk

## Funding information

Engineering and Physical Sciences Research Council, Grant/Award Number: EP/L014041/1

## Abstract

The rheology of non-Newtonian slurries is measured in a recirculating pipe loop using an acoustic velocimetry-pressure drop technique at very low flow rates and variable solids loadings. The technique avoids (a) settling at low solids concentration, a short-coming of bench rheometry, by using a vertical test section, and (b) physical sampling, providing greater safety. Speed of sound in the suspensions is also modeled. In-line and off-line data are used to assess the suitability of several non-Newtonian models to describe observed flow behavior. Measured and predicted values of the friction factor are compared with the Madlener et al Herschel–Bulkley extended model found to be superior. The dependence of yield stress and viscosity on solids loading and particle size is investigated, showing complexities from aggregation on the particle size distribution require more interpretation than the choice of rheological or friction-factor model.

## KEYWORDS

acoustic methods, Doppler velocimetry, in-line rheometry, multiphase flow, pipe flow

## 1 | INTRODUCTION

The need for sophisticated, data-rich but rapid and affordable in-line measurement for complex, multiphase flows exists across a range of industries, including high-value chemicals manufacturing, food and minerals processing, and waste/wastewater processing. This requirement is exacerbated when additional hazards are present, such as extreme temperature and pressure, chemical or corrosion hazards and radioactivity. The UK civil nuclear industry in particular has a mature and diverse inventory of active waste in storage, subject to processing and disposal, accumulated over the last six decades since the inception of the industry in the 1950s.<sup>1,2</sup> Much of this waste is chemically, physically, and rheologically complex,<sup>3–5</sup> and difficulties exist in understanding its composition and flow behavior due to hazards and limited accessibility. In the nuclear industry and beyond, there remains an

urgent, ongoing need for robust, easily deployed techniques with which operators can quickly characterize complex flows in a range of storage and transfer geometries. In a series of recent studies by the authors, a suite of acoustic techniques has been developed, specifically for: tracking of solids settling<sup>6,7</sup>; monitoring of settled bed resuspension by jet impingement<sup>8</sup>; solids volume fraction determination<sup>9–11</sup>; critical deposition velocity in pipe flow<sup>12,76</sup> and monitoring and categorization of moving beds of settled solids—that is, bedforms—in pipe flow.<sup>13</sup> Here the suite of methods is extended to in-line rheometry of complex slurries at low flow rates,  $3 \lesssim Re \lesssim 150$ , where the Reynolds number,  $Re$ , for non-Newtonian flows is defined later.

The rheological properties of complex, multiphase, and non-Newtonian flows are of central importance to operators for flow prediction and assurance, and in-line rheometry offers the potential for greater safety as the method precludes the need for sampling. Traditional tube

This is an open access article under the terms of the Creative Commons Attribution License, which permits use, distribution and reproduction in any medium, provided the original work is properly cited.

© 2020 The Authors. *AIChE Journal* published by Wiley Periodicals, Inc. on behalf of American Institute of Chemical Engineers.

rheometry<sup>14,15</sup> is well established and yields high-quality results<sup>16,17</sup> but requires precise characterization of fluid properties and entry conditions.<sup>18,19</sup> The method requires that the shear stress and shear rate be calculated from the measured pressure drop and volumetric flow rate, with the rheological parameters being derived by fitting to a suitable constitutive model.<sup>20,21</sup> A more recent variant of tube rheometry that employs velocimetry for determination of the shear rate, either via an acoustic method,<sup>22–24</sup> or via electrical resistance tomography and particle-image velocimetry,<sup>25</sup> has not found widespread industrial use. However, it offers the significant advantage over the traditional method that a single run yields a full rheological curve, that is, a set of viscosity data over a range of shear rates, as the shear rate varies across the pipe cross-section, rather than a single viscosity at a single shear rate determined from the mean flow velocity.<sup>26</sup> In-line rheometry satisfies the drive for minimally intrusive, remote, in-line measurement. It also addresses the trend for manufacturers to move toward in-line measurement, as high data acquisition rates are now possible for real-time product/formulation information, thereby avoiding physical sampling and, therefore, the possibility of altering the shear history of a suspension by sampling. Furthermore, in-line rheometry has the potential to be used to characterize suspensions at very low solids loadings that would otherwise settle in bench rheometers.

The main objective of this study is to assess the suitability of in-line rheometry via acoustic velocimetry for a range of complex, non-Newtonian slurry flows at low flow rates and low and intermediate solids fractions. Through this we extend the lower limit of the method in terms of Reynolds number ( $3 \lesssim Re \lesssim 150$ ). Suspensions of barium sulfate (barytes), calcium carbonate (calcite), and magnesium hydroxide were used. Rheological characterization is by application of several constitutive rheological models to these complex, non-Newtonian slurry flows.

We demonstrate a novel recirculating in-line pipe-loop method with a vertical test section that minimizes solids settling. This versatile apparatus can be used for any flowable suspension and avoids the shortcomings of other methods. We also compare the efficacy of two expressions from the literature for predicting the Fanning friction factor and therefore pressure drop, as the latter is required by operators for flow assurance and determining minimum pumping power requirements. The utility of the in-line rheometry technique is illustrated by assessing the influence of several measures of particle size on yield stress and effective mixture viscosity. To do this, the in-line data are compared to off-line bench rheometer data and modeled rheological parameters. With the friction factor modeling, the study provides a full methodology for monitoring slurries noninvasively, a key requirement for hazardous flows.

## 2 | MATERIALS AND METHODS

### 2.1 | Solid-phase characterization

Three solid particle species were used to form the suspensions—barytes, calcite, and magnesium hydroxide—and were chosen because

they are common nuclear waste analogues.<sup>4,11,27</sup> They have the additional benefits of being nonhazardous and widely available, and cover a range of material properties. The physical properties of the particle species (sources: barytes: RBH Ltd, Meriden, UK; calcite: Omya, Aberdeen, UK; magnesium hydroxide: Rohm and Haas, Surrey, UK) are summarized in Tables S1 and S2, including the bulk modulus and compressibility, which are used in the speed of sound correction referred to later. Samples were taken from the mixing tank before and after each run and allowed to settle for 7 days, at which point the bed packing fraction,  $\phi_m$ , in each sample was calculated from the height of the settled solids. Samples were not dried so that the settled solids retained any aggregates that may have formed. Mean values of  $\phi_m$  are also given in Table S1. Although not explicitly accounted for here, the shape of dry samples of the particle species has been investigated elsewhere. Barytes and calcite are both irregular-shaped milled minerals powders,<sup>28</sup> and calcite has been shown to aggregate to a small degree at neutral pH conditions.<sup>29</sup> Magnesium hydroxide consists of plate-like nanocrystalline agglomerated particles and exhibits complex behavior, forming fractal aggregates in suspension.<sup>4</sup>

Particle size distributions were measured with a Mastersizer 2000 laser diffraction instrument (Malvern Instruments, Malvern, UK). Samples of the solids species were mixed with a small amount of mains water to form a paste, several drops of which were added into a flow cell of the Mastersizer once it was filled with water and set to (a) agitate the mixing cell at 1800 rpm and (b) circulate through the measurement cell. The Mastersizer yields the volume- or mass-weighted mean particle diameter,  $d[3, 4]$ , but also the Sauter or area-weighted mean,  $d[2, 3]$ , and the 50th-percentile mean,  $d_{50}$ , for example, and a binned size distribution. The notation  $d[a,b]$  is a shorthand for the following:  $d[a,b] = m_a/m_b$ , where  $m_n$  is the  $n$ th moment of the particle size distribution such that, for a sampled size distribution with  $N$  size bins:

$$m_n = \sum_{i=1}^N w_i d_i^n, \quad (1)$$

where  $w_i$  is the weight/frequency of the  $i$ th bin. Expressions for determination of the mean,  $\mu$ , and standard deviation,  $\sigma$ , of a size distribution when modeled as a log-normal distribution are given in Data S1. Particle size data are shown in Figure 1 and summarized in Table S2, including  $d[2, 3]$  and  $d[3, 4]$  for completeness as these are commonly used measures for  $d_p$ .<sup>30,31</sup> Log-normal fits to the size data are also shown in Figure S1. The distributions given in Figure 1 represent the particle sizes in the dilute, well mixed limit. However, all three particle species, and calcite and magnesium hydroxide especially, may aggregate depending on the shear regime and pH level.<sup>4,29,32</sup> Calcite has been found to aggregate weakly at moderate pH, with a relatively low proportion of larger aggregates,<sup>29</sup> whereas aggregates larger than 100  $\mu\text{m}$  have been measured with similar magnesium hydroxide sludges under low-shear, settling conditions.<sup>4</sup> The aggregation, settling behavior and sediment compactness of barium sulfate in suspension has been found to be strongly influenced by pH<sup>32</sup>; it also has a surface charge that influences solid packing.<sup>11,33</sup>

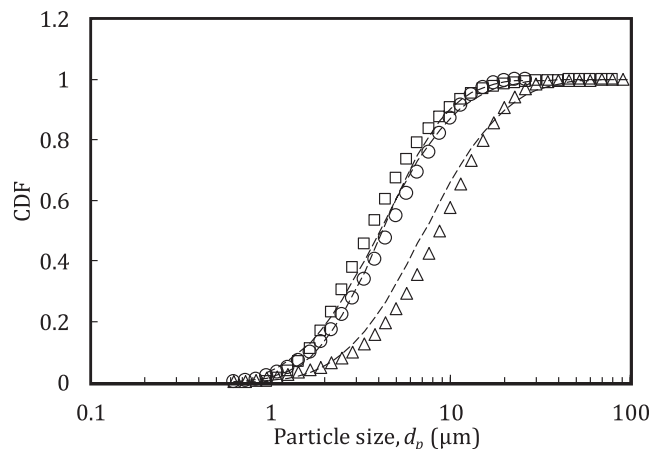


**FIGURE 1** Cumulative distribution function of particle size measured with Mastersizer instrument. Triangles: barium sulfate; circles: calcium carbonate; squares: magnesium hydroxide. Dashed lines: log-normal fits; fit parameters given in Table S2 in Data S1; see Figure S1 in Data S1 for goodness of fit

## 2.2 | Off-line rheometry

A Bohlin Gemini rheometer (Malvern Instruments, Malvern, UK) with a cup-and-vane geometry and controlled-stress configuration was used for the off-line rheometric measurements. The four-bladed vane with a diameter of 25 mm is shown in Figure S2, and the inner diameter of the cup was 37 mm, giving an operating gap<sup>3</sup> of 6 mm. The shear stress was varied over a range according to the properties of the suspensions determined during test runs and differed between particle species, and the shear rate measured. The yield stress,  $\tau_0$ , was found by nonlinear least-squares fit to  $\tau$  versus  $\dot{\gamma}$  via the Herschel-Bulkley (HB) model (i.e., Equation (5) with  $\eta_\infty = 0$ ), where  $\tau$  is shear stress and  $\dot{\gamma}$  is shear rate. It is noted that  $\tau_0$  was also determined with a different method from in-line measurements; both sets of results are compared later. The infinite-shear viscosity,  $\eta_\infty$ , was taken as the minimum value of  $\eta$ .

## 2.3 | Pipe flow loop and in-line rheometry

A commercial ultrasonic system<sup>34</sup> was used for velocimetric measurement consisting of a UVP-DUO signal processor (Met-Flow, Lausanne, Switzerland) and a monostatic (i.e., emitter-receiver) transducer operating at 2 MHz (Imasonic, France) directed upstream to reduce flow interference, at 45° to the flow, with a spatial resolution of 0.5 mm. The piezoelectric transducer (8 mm outer diameter, 5 mm active) is excited by a voltage with a user-defined duration, fundamental frequency and repetition frequency, thereby emitting an acoustic pulse. Particles in the flow reflect some of the acoustic energy through scattering and this excites a voltage in the transducer.<sup>35,36</sup> The UVP-DUO instrument performs a fast Fourier transform on segments of the voltage time series to calculate the frequency of the received signal as a function of distance from the transducer. The difference between the

emitted and received frequencies is found via the Doppler equation, as the speed of sound in the suspension is known (and precisely modeled, as described later), so the velocity of particles at a particular position in the flow field can be calculated.<sup>37</sup>

Pressure transducers (Omega Engineering, Manchester, UK) positioned at an interval of 50 cm were used to measure the pressure drop, and a strain valve was used to maintain positive pressure at the sensor positions. The pressure and acoustic transducers were mounted on a test section of a recirculating pipe flow loop with an inner diameter of  $D = 42.6$  mm. The test section was orientated vertically to minimize radial variation in solids concentration, velocity, and particle concentration fields. In addition, the diameter of the test section was larger than that in the rest of the flow loop (28.4 mm) in order to produce a higher flow rate outside the test section and discourage settling of solids and depletion of the nominal solids volume fraction.

The experimental apparatus is shown in Figure S3. A variable centrifugal pump (Ebara Pumps, Didcot, UK) was used to control the flow rate and a mixer with impeller to maintain a suspension in the mixing tank (nominal capacity 40 liters).

### 2.3.1 | Pressure drop measurement

The vertical configuration of the test section of the flow loop dictated that a correction for hydrostatic pressure be applied to the recorded pressure drop, such that  $\Delta P = \Delta P_m - \rho g \Delta h$ , where  $\Delta P_m$  is the measured pressure drop between two pressure transducers and the second term is the hydrostatic correction, where  $\rho$  is the suspension density,  $g$  is the acceleration due to gravity, and  $\Delta h$  is the vertical distance between measurement points (i.e.,  $\Delta h = L = 0.5$  m). The suspension density was calculated using the data sources given in Table S1. The temperature,  $T$ , was measured from the mixing tank during each run and was accounted for in the water density, as given in Table S1, when evaluating  $\Delta P$ .

### 2.3.2 | Velocity and flow rate measurement

Compressibility data given in Table S1, along with density data, were used to correct (a) distance and (b) velocity measurements taken with the acoustic instrument (since both require the speed of sound to be specified); the process is described in the “Speed of sound variation” section of Data S1, specifically Equation (S10) onwards. As with density, temperature variation was accounted for in the compressibility of water as given in Table S1, but not for the solid species, for which single, temperature-independent values were used.

The HB rheological model incorporates yield stress and power-law terms, while the HB extended (HBE) model also includes an infinite-shear viscosity term; both are described in detail in the next section. Analytical expressions for the velocity distribution in Poiseuille (i.e., cylindrical pipe or tube) flow in the HBE case are not available, but in the HB case they are as follows<sup>38,39</sup>:

$$U_{\max} = \left(\frac{\tau_w}{K}\right)^{\frac{1}{n}} \frac{R}{\left(\frac{1}{n} + 1\right)} \left(1 - \frac{\tau_0}{\tau_w}\right)^{\frac{1}{n} + 1}, \quad 0 < r \leq r_p, \quad (2)$$

$$U(r) = \left(\frac{\tau_w}{K}\right)^{\frac{1}{n}} \frac{R}{\left(\frac{1}{n} + 1\right)} \left[ \left(1 - \frac{\tau_0}{\tau_w}\right)^{\frac{1}{n} + 1} - \left(\frac{r - \tau_0}{R - \tau_w}\right)^{\frac{1}{n} + 1} \right], \quad r_p \leq r < R, \quad (3)$$

where  $U_{\max}$  is the velocity in the central plug region that is a result of the yield stress and  $r_p$  is the plug radius, within which the mixture flow velocity is constant. The shear stress,  $\tau$ , varies linearly with radial position, according to  $r/R = \tau(r)/\tau_w$ , where  $\tau_w$  is the wall shear stress. As in the flow of any yield-stress substance, the plug radius corresponds to that at which the shear stress equals the yield stress, such that  $r_p/R = \tau_0/\tau_w$ . The wall shear stress is inferred from the measured pressure drop according to  $\tau_w = D\Delta P/4L$ , where  $D$  is the inner pipe diameter ( $D = 42.6$  mm). The Fanning friction factor,  $f$ , is calculated according to  $f = 2\tau_w/\rho\bar{U}^2$ , where  $\bar{U}$  is the bulk flow velocity such that  $Q = \bar{U}A$ , where  $Q$  is the volumetric flow rate and  $A = \pi D^2/4$  is the cross-sectional flow area. According to the Poiseuille friction law for laminar flow,  $f = 16/Re$ , where  $Re$  is the Reynolds number such that, in the Newtonian case,  $Re = \rho\bar{U}D/\eta$ . A long-standing question exists as to which formulation of the Reynolds number is most suitable if the relationship  $f = 16/Re$  is to be valid in the case of non-Newtonian flows.<sup>20</sup> The ability of two models<sup>40,41</sup> to predict frictional losses is described in the friction factor modeling section; both are given in Data S1.

The shear stress distribution varies linearly with radial position according to  $r_p/R = \tau_0/\tau_w$  and was determined from the measured pressure drop,  $\Delta P$ , via the relationship  $\tau_w = D\Delta P/4L$  and the shear rate from the velocity field measured with the ultrasonic system as follows<sup>42</sup>:

$$\dot{\gamma}(r) = -\frac{d\bar{U}(r)}{dr}. \quad (4)$$

The suspension viscosity,  $\eta(r)$ , was then calculated according to  $\tau = \eta\dot{\gamma}$ . This is illustrated in the results section in Figure 4 for velocimetric data, which is transformed into rheometric data via the expressions above, as illustrated in Figure 5. The volumetric flow rate,  $Q$ , was measured by numerical integration of the velocity field as measured with the acoustic system (see Figure S4 and associated text in Data S1). The flow loop was filled with suspensions at several nominal (weighed) concentrations,  $\phi_n$ , to verify mixing efficiency. Samples were taken from the mixing tank after the suspension had been circulated for 1 min at a low flow rate. A comparison of nominal and physically sampled volume fractions,  $\phi_s$ , is shown in Figure S5 of Data S1, from which it is clear that calcite and magnesium hydroxide remained almost fully suspended at all volume fractions, whereas barytes, having a significantly higher material density, were depleted relative to the nominal volume fraction (by 50, 56, 64, 26, and 12% at  $\phi = 0.5, 1, 2, 5,$  and  $10\%$ , respectively). However, measured—rather than nominal—values of the volume fraction were used in all calculations.

### 2.3.3 | Determination of rheological parameters

The constitutive equation in terms of shear stress, applied shear rate,  $\dot{\gamma}$ , where  $\dot{\gamma} = dy/dt$ , and apparent viscosity,  $\eta$ , for the HBE model are, respectively<sup>41</sup>:

$$\tau_{\text{HBE}} = \tau_0 + K\dot{\gamma}^n + \eta_{\infty}\dot{\gamma}, \quad (5)$$

$$\eta_{\text{HBE}} = \tau_0\dot{\gamma}^{-1} + K\dot{\gamma}^{n-1} + \eta_{\infty}, \quad (6)$$

where  $\tau_0$  is the yield stress,  $n$  is the flow index or viscosity index,  $K$  is the consistency index,  $\eta_{\infty}$  is a limiting viscosity at high shear rates sometimes referred to as the Bingham or infinite-shear viscosity. The HBE model, based on previous models of non-Newtonian flow,<sup>43,44</sup> differs from the HB model,<sup>38</sup> in that it includes  $\eta_{\infty}$ , potentially allowing a greater range of materials to be characterized than with the HB model. Expressions that allow yield stress and effective suspension viscosity to be predicted based on particle size and concentration are presented and discussed in the results section.

The velocimetry system used in this study allowed for rheological parameters to be calculated in two ways: first, directly by fitting the recorded mean velocity profile (see Equation (7)); and second, by a fit to a rheological curve via Equation (4) for  $\tau$  and  $\dot{\gamma}$ . These methods are treated as distinct because they yield different values for the rheological parameters and rely on different fitting procedures, and are summarized in Figure 2. Both in-line and off-line methods are used to measure some rheological parameters and, depending on which are known, either the HB or HBE model is used to determining the remaining parameters.

In the velocimetric case (i.e., Method 1, Figure 2), by using Equations (2) and (3), the following expression is obtained for the mean axial velocity profile in the HB case:

$$\frac{U(r)}{U_{\max}} = 1 - \left(\frac{\frac{r - \tau_0}{R - \tau_w}}{1 - \frac{\tau_0}{R - \tau_w}}\right)^{\frac{1}{n} + 1}, \quad r_p \leq r < R. \quad (7)$$

A value for the plug radius,  $r_p$ , was determined by visual inspection of the velocity profile;  $\tau_0$  could then be found, as  $r_p/R = \tau_0/\tau_w$ , and  $U_{\max}$  was calculated as the mean value of  $U(r)$  for  $r < r_p$ . The parameter  $n$  was then found by nonlinear fit of the data to Equation (7) for  $r > r_p$ ;  $K$  was then calculated from Equation (2). A velocimetric method like Method 1 cannot be used with the HBE model, as no analytical expression for the velocity field exists for that model. However, velocimetric data can be converted into rheometric data via Equation (4) and used with either the HBE model (if  $\eta_{\infty}$  is known) or the HB model (if  $\eta_{\infty}$  is not known). Equation (5) can be recast in the HBE and HB cases, respectively, such that:

$$\ln(\tau - \tau_0 - \eta_{\infty}\dot{\gamma}) = \ln K + n \ln \dot{\gamma}, \quad \tau > \tau_0 + \eta_{\infty}\dot{\gamma}, \quad (8)$$

$$\ln(\tau - \tau_0) = \ln K + n \ln \dot{\gamma}, \quad \tau > \tau_0, \quad (9)$$

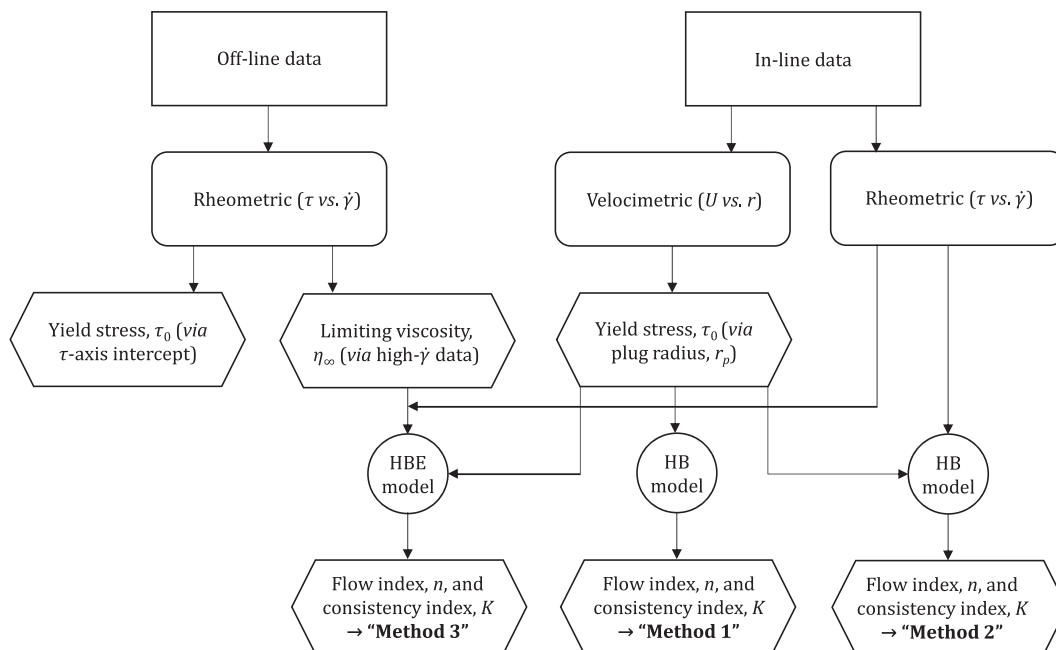


**FIGURE 2** Flowchart for determination of rheological parameters

where  $\dot{\gamma}$  and  $\tau$  are calculated from the recorded velocity profile and pressure drop, respectively. The infinite-shear viscosity,  $\eta_{\infty}$ , was determined from the off-line data and  $\tau_0$  in-line via  $r_p/R = \tau_0/\tau_w$ ;  $n$  and  $K$  were then found by fitting Equation (8) (HBE case) or Equation (9) (HB case) to the  $\tau$  versus  $\dot{\gamma}$  data. These rheometric methods are referred to hereafter as Method 2 in the HBE case and Method 3 in the HB case as shown in Figure 2.

## 3 | RESULTS AND DISCUSSION

### 3.1 | Off-line rheometry

Off-line rheometric data are shown in Figure S6 of Data S1 for the three particle species. We used a nonlinear least-squares fit to the HB model to estimate the yield stress and the other rheological parameters, and we note that some data at (a) very low and (b) very high shear rates were excluded from the fits (data selections are given in Table S3) because (a) some were deemed as falling below the sensitivity of the bench rheometer and (b) the HB model cannot account for high-shear-rate behavior in the presence of a limiting viscosity. At all volume fractions, the fit is good and the yield stress is taken as the  $\tau$ -intercept. A relatively low degree of hysteresis between the upward and downward shear stress ramping is noted in most datasets, likely due to suspension network rearrangement or additional load stresses in the gel samples.

Off-line rheometric data (in  $\eta$  vs.  $\dot{\gamma}$  form) are presented in Figure 3 for the three particle species for determination of the infinite-shear viscosity,  $\eta_{\infty}$ . It is noted that the upward and downward sweeps of shear stress applied to the suspensions by the rheometer

are indicated by arrows for one run only, to avoid cluttering the plots. The upper arm of data is always the upward sweep. Generally, all suspensions are strongly shear thinning, as would be expected.<sup>45-48</sup> Interestingly, the relative shear viscosity of the calcite and magnesium hydroxide suspensions are both an order of magnitude larger than the barytes for a given concentration. This difference indicates a degree of aggregation (and higher associated drag) in the case of the calcium carbonate and magnesium hydroxide suspensions, increasing the viscosity relative to the more discrete barytes (as anticipated and as discussed within the methodology).<sup>4,11,29,32,33,49</sup> It is noted, in fact, that barytes did not remain suspended in the rheometer cell at  $\phi = 10\%$ , as sedimentation caused significant hysteresis in the data, and therefore these data are not shown. This serves to illustrate the superior capability of in-line rheometry, particularly in a vertical flow orientation, as depletion of the solid phase across the measurement domain is completely eliminated.

### 3.2 | In-line rheometry

Velocity profiles at  $\phi = 10\%$  are presented in Figure 4, in order to illustrate the goodness of fit with Equation (7) and as examples of Method 1 (see Figure 2). The goodness of fit compares very well with similar studies of velocimetry for in-line rheometry.<sup>23,50,51</sup> Error bars are shown for every fifth datum and represent the standard deviation over 3,000 samples (119 ms sample period, i.e., 6 min total). Figure 4 also serves to demonstrate the advantage that velocimetric in-line rheometry has over traditional tube rheometry in that a full rheological curve is produced from a run at a single flow rate. Included in the plots are velocity profiles of equivalent Newtonian flows with the

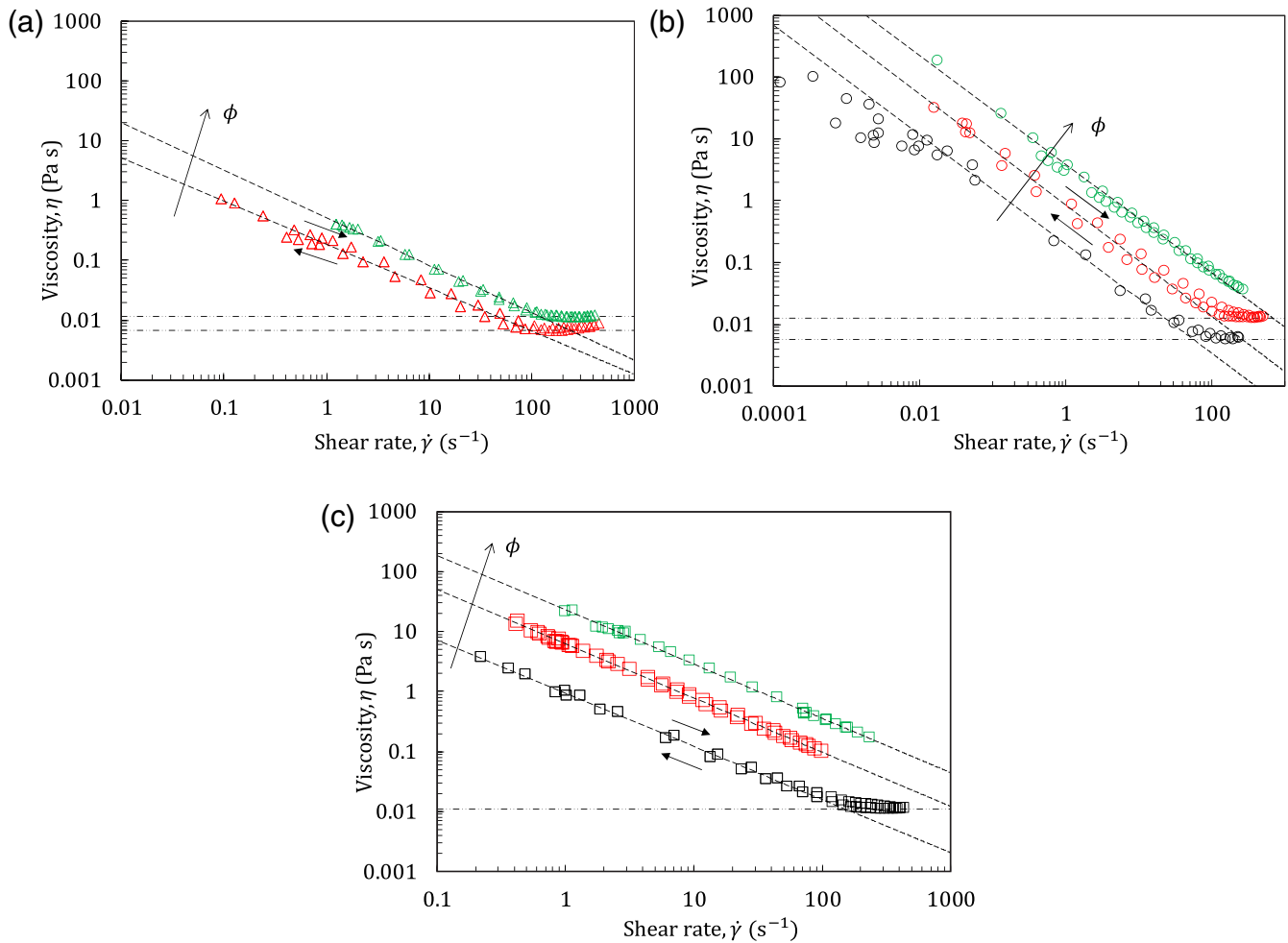


**FIGURE 3** Off-line rheometric data for (a) barium sulfate (triangles), (b) calcium carbonate (circles), and (c) magnesium hydroxide (squares). Black, red, and green markers:  $\phi = 10, 15,$  and  $20\%$ , respectively. Dashed lines: power-law fits,  $\dot{\gamma} < 100 \text{ s}^{-1}$  only, for visualization of trends. Dashed-dotted lines:  $\eta_{\infty}$ , taken as minimum (where present in data) of  $\eta$ . Arrows parallel to data indicate upward and downward sweeps in stress-controlled experiments; only shown for one run for clear visualization [Color figure can be viewed at [wileyonlinelibrary.com](http://wileyonlinelibrary.com)]

same values of the flow rate,  $Q$  (and therefore bulk flow velocity), and pressure drop (and therefore wall shear stress);  $U_e$  is parabolic such that:

$$U_e(r) = \frac{|\Delta P|}{4\eta_e L} (R^2 - r^2) = \frac{\tau_w}{2\eta_e R} (R^2 - r^2), \quad (10)$$

and  $U_{e,\max} = U_e(r = 0) = \tau_w R / 2\eta_e$ , where  $\eta_e$  is the viscosity of an equivalent Newtonian fluid. The flow rate is as follows:

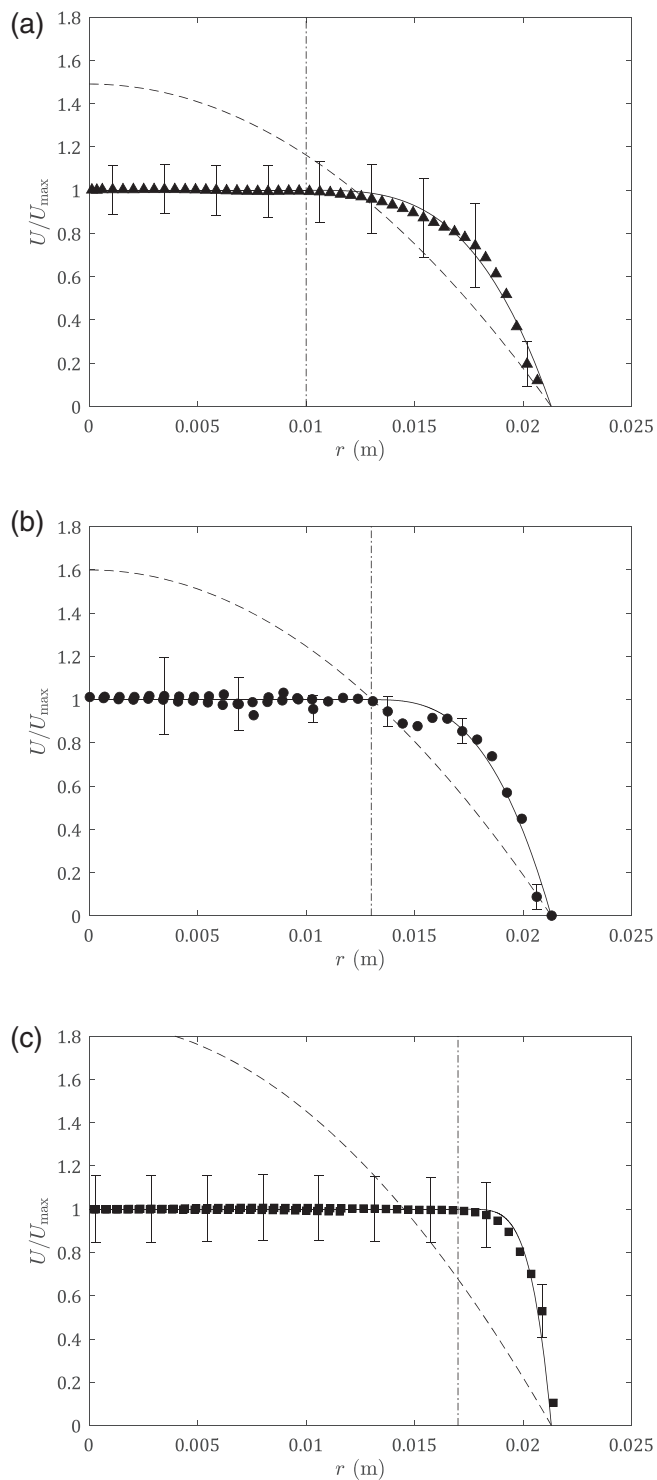
$$Q = \frac{\pi R^4 |\Delta P|}{8\eta_e L} = \frac{\pi \tau_w R^3}{4\eta_e}. \quad (11)$$

It is clear that the non-Newtonian flows investigated here—all of which are shear-thinning at shear rates up to at least  $\dot{\gamma} = 100 \text{ s}^{-1}$ —exhibit significantly lower centreline velocities than for equivalent Newtonian flows, as is expected because laminar, Newtonian flows show a parabolic velocity profile.<sup>52</sup> Rheometric data in  $\eta$  versus  $\dot{\gamma}$  form, derived from both in-line velocimetric data and from off-line

measurements, are compared in Figure 5 at  $\phi = 10\%$ . No off-line data are compared for the case of barium sulfate, as a stable suspension could not be maintained in the off-line rheometer, as discussed. In Figure 5, as elsewhere, off-line data are indicated by open symbols, and all in-line data by closed symbols. Gray in-line data are those that did not satisfy Equation (9), that is, fell within the plug radius of the flow, so could not be used for fitting to the HB (or HBE) model. It is noted that some in-line data could not be used for the fit to the HBE model as they did not satisfy Equation (8).

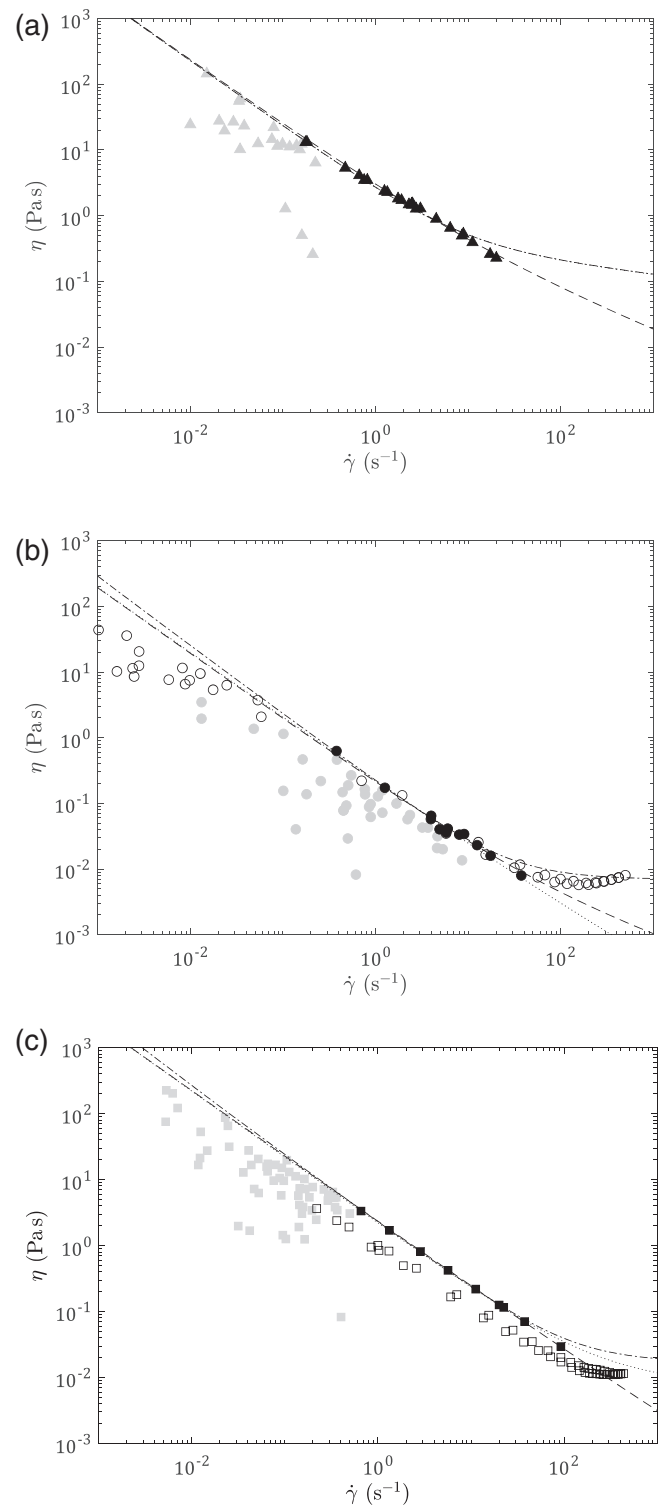
Several observations can be made from Figure 5: (a) that all three fits (Method 1, i.e., HB case, velocimetric; Method 2, i.e., HB case, rheometric; Method 3, i.e., HBE case, rheometric) are very good at least in the range  $\dot{\gamma} < 10 \text{ s}^{-1}$ , with one fit diverging from the others at higher shear rates (Method 3, i.e., HBE case,  $\dot{\gamma} > 10$ ), as expected, because of the infinite-shear viscosity in that model.

Figure 5 serves to illustrate the effectiveness of the in-line method relative to (a) bench-based, off-line rheometric methods (which may suffer from settling of solids in the measurement cell at



**FIGURE 4** Velocity profile of suspensions, all at  $\phi = 10\%$ ; (a) barium sulfate (triangles), (b) calcium carbonate (circles), and (c) magnesium hydroxide (squares). Circles: in-line velocimetry data; solid line: fit via Equation (7); dashed line: profile of equivalent Newtonian flow via Equation (10); vertical dashed-dotted line: plug radius,  $r_p$ . Error bars shown for every fifth datum

low concentrations), and (b) traditional tube rheometry (which yields only a single datum per run). Figure 5 also shows the limitation of this approach which, although not severe in the runs performed here,



**FIGURE 5** Viscosity of suspensions, at  $\phi = 10\%$ ; (a) barium sulfate (triangles), (b) calcium carbonate (circles), (c) magnesium hydroxide (squares). Open symbols: off-line data (none given for barium sulfate due to settling in rheometer); closed symbols: in-line data. Dashed line: HB case, fit to velocimetric data (Method 1); dotted line: HB case (i.e.,  $\eta_\infty = 0$ ), fit to rheometric data (Method 2); dashed-dotted line: HBE case, fit to rheometric data (Method 3). Gray symbols: in-line data not satisfying Equation (9) and therefore not used in fits. HB, Herschel-Bulkley; HBE, Herschel-Bulkley extended

dictates that the higher the yield stress, the narrower the region (specifically the region  $r_p > r > R$ ) in which Equation (9) is satisfied and the fewer data that can therefore be used in a fit. The criterion is stricter still for the HBE case (i.e., Equation (8)).

Lastly, the runs shown in Figure 5b,c were chosen because in these cases both in-line and off-line data were available. The agreement between the off-line (open symbols) and in-line data (closed symbols) is excellent for calcium carbonate (Figure 5b,  $\phi = 10\%$ ) and good for magnesium hydroxide (Figure 5c,  $\phi = 10\%$ ). Similarly good agreement has been found by several other researchers using, for example, xanthan gum suspensions and a polynomial fit to the velocity profile<sup>53</sup>; several flowable food suspensions<sup>42</sup> and wastewater sludge<sup>50</sup> and a HB fit (as used here, see Equations (2) and (3)); polymer gels<sup>51</sup>; and polymer melts<sup>54</sup> with an Eyring-type velocity fit.<sup>55</sup> In most cases, discrepancies between data obtained using in-line and other methods are of the order of tens of percent, as here, which is encouraging, since an objective of this study was to operate at lower flow rates ( $3 \lesssim \text{Re} \lesssim 150$ ) than had been achieved in other studies—for example,  $\text{Re} = 320$ , Kotzé et al<sup>50</sup>—in order to test the limit of the method.

### 3.3 | Friction factor modeling

For the expression  $f = 16/\text{Re}$  to hold in non-Newtonian suspensions, a variety of expressions exists for substances obeying, for example, the power-law<sup>56</sup> and HB<sup>57</sup> relationships. A commonly used model suitable for the HB and lesser cases is that of Chilton and Stainsby.<sup>40</sup> A recent analytical solution for the general HBE case was presented by Madlener et al.<sup>41</sup> In order to examine the suitability of these models (see Data S1) for determination of the Fanning friction factor,  $f$ , in non-Newtonian flows, the models are applied to all data from the present study. The friction factor is important for operators when calculating the minimum necessary pumping power, for example, and relates the applied pressure or hydraulic head to the resulting flow velocity. Values of  $f$  using the relationship<sup>17</sup>  $f = 2\tau_w/\rho U$  are plotted in Figure 6 against predictions from the relationship  $f = 16/\text{Re}$  using values of  $\text{Re}$  calculated from Equation (S13) of Data S1 in the case of the Chilton and Stainsby<sup>40</sup> model and Equation (S16) in the case of Madlener et al<sup>41</sup>; all friction factor data are given in Table S4 of Data S1. For fit (1) in Figure 6—HB model, fit to in-line velocimetric data—the agreement is very good and equally so for the Chilton and Stainsby<sup>40</sup> and Madlener et al<sup>41</sup> models. For fit (2)—HB model, fit to in-line rheometric data—the agreement is less good than fit (1) and for the Chilton and Stainsby<sup>40</sup> model. In Case (2), the ratio,  $r_f$ , of predicted to measured values of  $f$  was  $0.67 \leq r_f \leq 1.49$  for the Chilton and Stainsby model and  $0.90 \leq r_f \leq 1.10$  for the Madlener et al model. For fit (3)—HBE model, fit to in-line rheometric data with infinite-shear viscosity from off-line data—the agreement is also very good, although in this case only the Madlener et al<sup>41</sup> model could be used as the Chilton and Stainsby<sup>40</sup> model does not incorporate the infinite-shear viscosity,  $\eta_\infty$ .

On the basis of the results presented in Figure 6, the Madlener et al<sup>41</sup> model is recommended as (a) it appears to make more accurate

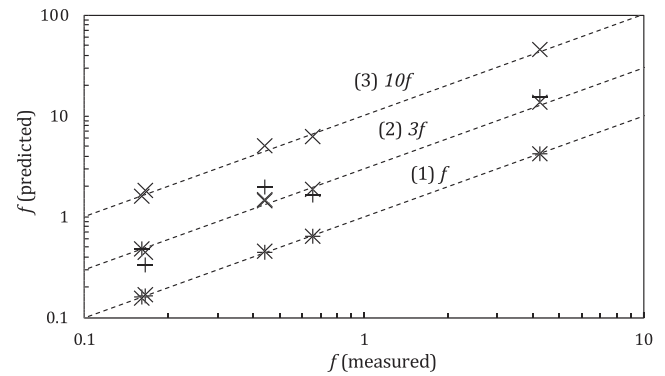


**FIGURE 6** Comparison of predicted and measured friction factor,  $f$ . Offsets for clear visualization: (1) HB model, fit to in-line velocimetric data; (2) HB model, fit to in-line rheometric data; (3) HBE model, fit to in-line rheometric data with infinite-shear viscosity from off-line data. Pluses: prediction of Chilton and Stainsby<sup>40</sup>; crosses: prediction of Madlener et al.<sup>41</sup> Dashed line: one-to-one relation. All friction factor data given in Table S4 of Data S1. HB, Herschel–Bulkley; HBE, Herschel–Bulkley extended

predictions, and (b) it can account for more complex rheological behavior through the infinite-shear viscosity term of the HBE case. However, if the infinite-shear viscosity is not known (as is more likely to be the case at low flow rates without off-line characterization), the Chilton and Stainsby<sup>40</sup> and Madlener et al<sup>41</sup> models perform equally well if velocimetric data are used.

### 3.4 | Yield stress and relative viscosity modeling

Thomas<sup>16,17</sup> applied the Bingham plastic model to capillary-tube rheometry data using a range of particle species and found that the following expressions for the yield stress and (Bingham) viscosity, respectively, provided good fits to the data:

$$\tau_0 = k_1 \phi^3 = 10,055 d_p^{-2} \phi^3, \quad (12)$$

$$\eta_{\infty,r} = \frac{\eta_\infty}{\eta_f} = \exp(k_2 \phi) = \exp\left[\left(2.5 + 14 d_p^{-0.5}\right) \phi\right], \quad (13)$$

where  $\phi$  is the dry-weight volume fraction of suspended solids,  $d_p$  is a representative particle diameter, and  $\eta_f$  is the viscosity of the fluid phase. The general forms of the expressions, which can be found by allowing the numerical terms to vary, are given in Equations (14) and (15). They allow rheological properties to be predicted based on particle size and concentration, but particle shape and aggregation state are not explicitly accounted for:

$$\tau_0 = a_1 d_p^{b_1} \phi^3, \quad (14)$$

$$\eta_{\infty,r} = \exp\left[\left(2.5 + a_2 d_p^{b_2}\right) \phi\right]. \quad (15)$$

Measured values of the yield stress and relative viscosity from this study are presented in Figure 7. Both in-line and off-line data were available for yield stress (Figure 7a), whereas for relative

viscosity (Figure 7b) all data are from off-line measurements, as the flow rates in the in-line experiments were too low to determine  $\eta_{\infty}$  at  $\phi = 10\%$ . However, in-line and off-line viscosity at a shear rate of  $\dot{\gamma} = 10 \text{ s}^{-1}$  are given in Table S5 in Data S1. As described in Equation (14) for yield stress, the fit lines in Figure 7a vary as  $\phi^3$ , and as in Equation (15) for relative viscosity, the fit lines in Figure 7b vary according to  $\exp(k_2\phi)$ .

It is clear from Figure 7a that for the magnesium hydroxide and calcium carbonate systems, the yield stress values are largely consistent between off-line and in-line data, and follow the expected  $\tau_y \propto \phi^3$  dependence (see Equation (14)), although off-line measurements for magnesium hydroxide are slightly below those measured in-line. This difference may simply be due to the different qualities of fits for yield stress values between the techniques, given the low levels of yield stress overall in these systems (and thus higher degree of fit uncertainty). The discrepancy for the barytes yield stress data is larger, with the in-line measurement for the  $\phi = 10\%$  system being around an order of magnitude larger than the off-line value for the  $\phi = 15\%$  suspension. It is noted again that no off-line data were available for the  $\phi = 10\%$  systems, as clear evidence of sedimentation was present in the rheometer cell. Although the  $\tau_0 = 2 \text{ Pa}$  value determined from the in-line data may suggest the suspension is above the gel-point, it may be that due to the highly dense nature of barytes, the lithostatic load is great enough to overcome the correspondingly low yield strengths, leading to compressional collapse at this concentration. Also, the very low yield stress apparent in the off-line data at  $\phi = 15\%$  may indicate that some degree of settling or network consolidation occurred in this system (and may explain some of the hysteresis in these data; see Figure S6 in Data S1).

Nonetheless, there is no strong evidence for significant settling from the off-line infinite-shear viscosity data (Figure 7b) where all systems display the expected dependence (see Equation (15)), which are given for completeness and to illustrate trends. Any considerable settling within certain systems (e.g., barytes at 15%) would lead to a reduction in reported viscosity values. In addition, the viscosity of

magnesium hydroxide and calcite systems were compared between off-line and in-line techniques at a shear rate  $\dot{\gamma} = 10 \text{ s}^{-1}$ ; see Table S5. Again, the correlation between the two techniques is close, especially for the calcite suspensions, highlighting the performance of the in-line method for accurately measuring flow behavior and secondarily giving confidence of the data quality for off-line measurements.

Broadly, both the yield stress and viscosity results confirm that aggregation plays a dominant role in the rheological behavior of these suspensions. With the exception of the in-line measurements for magnesium hydroxide and barium sulfate, which are similar in magnitude, the trends are for both yield stress (particularly in the off-line measurements) and effective viscosity to increase strongly with a tendency to aggregate: magnesium hydroxide is most strongly aggregated, then calcium carbonate, then barium sulfate. This trend can also be viewed from the perspective of solids packing fraction. Samples were taken from the mixing tank (approximately 60 ml each) and allowed to consolidate under gravity for 7 days. Mean values of the mean bed packing fraction,  $\phi_m$ , in the settled (wet) samples are given in Table S1 in Data S1, where it is noted that the value for magnesium hydroxide ( $\phi_m = 8.4\%$ ) is very close to that measured by Johnson et al<sup>4</sup> for the same material using two methods ( $\phi_m = 7.5$  and  $7.8\%$ ); different measurement methods accounting for the difference. With reference to the rheometric results described above, there is a strong inverse correlation between bed packing fraction and measured rheological parameters in the off-line results. The species with the lowest packing fraction (magnesium hydroxide) has the highest yield stress and viscosity at a given solids loading. We note that the more likely a particle species is to form an aggregate network, the lower its bed packing fraction,<sup>4,11,29,32,33,49</sup> although this conclusion requires further testing.

The values of the fit parameters  $k_1$  and  $k_2$  (for the yield stress and relative viscosity, via Equations (14) and (15), respectively) are listed in Table S6 in Data S1. The calculated values of  $k_1$  and  $k_2$  were used to

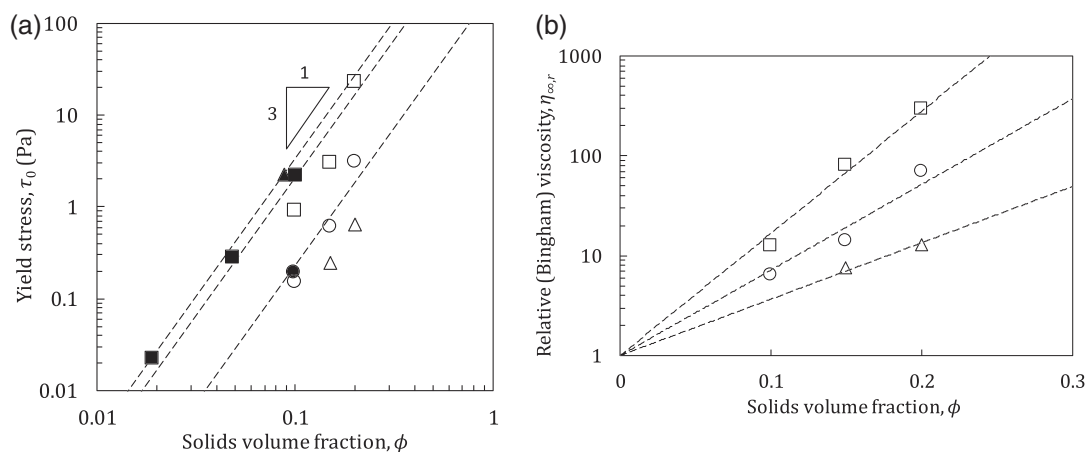


**FIGURE 7** (a) Yield stress and (b) relative viscosity versus solids volume fraction. Triangles: barium sulfate; circles: calcium carbonate; squares: magnesium hydroxide. (a) Filled symbols: in-line results via velocimetry; open symbols: off-line results via fit to off-line shear rate–shear stress data (excluded from fit for barium sulfate due to settling in the off-line rheometer); (b) all off-line data. Dashed lines: fits via (a) Equation (14) (in-line results only) and (b) Equation (15)

derive the fit parameters  $a_1$ ,  $b_1$  (for yield stress via Equation (14)),  $a_2$  and  $b_2$  (for relative viscosity via Equation (15)) for each choice of the particle size measure  $d_p$ ; in particular,  $d_p$  was chosen to be one of the following:  $\mu$  (i.e.,  $m_1$ ),  $d_{50}$ ,  $d[2, 3]$  and  $d[3, 4]$ , which are listed in Table S2 in Data S1. The resulting fits are shown in Figure 8 for relative viscosity and Figure S7 in Data S1 for yield stress ( $d_p = d[2, 3]$  and  $d_p = d[3, 4]$  not shown, for clarity of visualization); the fit parameters are listed in Table 1.

It is clear from these fits that the dependences on particle size and solids volume fraction assumed by Thomas,<sup>16,17</sup> indicated by dashed-dotted lines in Figures S7 and 8 and given in Equations (12) and (13), respectively, although based on physical arguments, perform worse than if the fit parameters are allowed to vary freely. Several aspects of the results are notable: (a) the dependence of yield stress and viscosity on  $d_p$  varies with the choice of  $d_p$ ; and (b) the exponent  $b_1$  is positive for every choice of  $d_p$ , meaning that yield stress increases with particle size—which disagrees with the findings of Thomas<sup>16,17</sup>—and  $b_2$  is negative—which is in agreement with Thomas.<sup>16,17</sup> Zhou et al<sup>58</sup> found a  $\tau_y \propto d_p^{-2}$  dependence in alumina suspensions, but also noted that there is no broad agreement as to the nature of the relationship between yield stress and mean particle size—or particle size distribution<sup>59</sup>—with some studies finding an inverse relationship with  $d_p$ ,<sup>60</sup> and others inverse square<sup>16,61</sup> or inverse cubic.<sup>62</sup> It can be concluded from the results shown in Figures 8 and S7 that knowledge of particle size alone is not sufficient to understand the rheology of complex suspensions that deviate from ideal, hard-sphere (i.e., noninteracting) behavior.

While some studies also predict a floc-size (rather than individual particle-size) dependence,<sup>63–65</sup> others suggest floc size is not the most important property for predictive purposes.<sup>66,67</sup> Viamajala et al<sup>68</sup> found that the yield stress and (shear-thinning) viscosity of corn stover-water slurries increased with solids concentration and particle

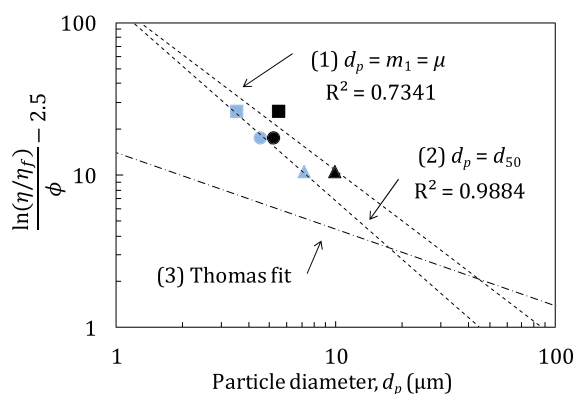


**FIGURE 8** Dependence of relative viscosity on solid particle diameter. (1) Black markers:  $d_p = m_1 = \mu$ ; (2) light blue markers:  $d_p = d_{50}$ ; triangles: barium sulfate, circles: calcium carbonate, squares: magnesium hydroxide. Dashed lines: power-law fits; (3) dashed-dotted line: Equation (13) from Thomas.<sup>16,17</sup> Fits for  $d_p = d[2, 3]$  and  $d[3, 4]$  not shown to allow clear visualization; all fit parameters given in Table 1 and Table S6 in Data S1 [Color figure can be viewed at [wileyonlinelibrary.com](http://wileyonlinelibrary.com)]

size. Ancy and Jorrot<sup>69</sup> found that, in clay suspensions, mean particle size had little effect on the yield stress. However, in bimodal suspensions the effect was (a) strong and (b) depended on the relative amounts of fine and coarse particles, in agreement with the results of Banfill<sup>59</sup> with sand suspensions and Singh et al<sup>70</sup> with coal slurries. It is reasonable, more generally, to conclude that the dependence on particle/floc sizes may fall under two broad patterns, based on the size regime. For very large, noncohesive granular material, yield stress is dominated by particle contact inertia, and may therefore be assumed to increase with the size of the particles. For fine colloidal materials, where surface forces dominate, the cohesive suspension yield stress often increases with the surface area to volume ratio, as an inverse to particle size, as found elsewhere.<sup>16</sup> For the suspensions considered here, the complication of aggregation and increasing size distribution is present, and more explicit knowledge of the relative aggregate size distributions of the suspensions (rather than the disperse primary particle sizes) may aid understanding. However, it is also interesting that the correlation between relative viscosity and particle size is stronger than that for yield stress, and is in line with expectations, that is, that smaller particles at a given volume fraction, which therefore have a greater number density, will increase the overall fluid resistance to flow to a greater degree than larger particles.

Nevertheless, it is clear from the above discussion that particle size alone—when represented by a single measure,  $d_p$ —is not sufficient when used to model yield stress and relative viscosity, in so far as different choices for  $d_p$  yield entirely different dependences. A particular dependence may shed light on which physical process is dominant, but the observed ambiguity makes such an identification impossible. Such ambiguity was also found by Li et al,<sup>71</sup> depending on whether number-, surface- or volume-weighted mean particle sizes were used. However, the effective particle size—from a rheological point of view—depends strongly on the aggregation state, which in general depends strongly on the solids concentration. Moreover, the method used for particle sizing may differ from the aggregate size at high solids loadings. For example, both sedimentation (i.e., wet sample) and electron micrography (i.e., dry sample) were used for particle sizing by Thomas<sup>16</sup> and in the present study a very dilute suspension was used, albeit in a wet cell of a laser diffraction sizing instrument.

It is suggested that, as well as some measure of particle size in whatever form (e.g.,  $d_{50}$ ), at least two other properties of the solid phase be given equal consideration: (a) the width of the particle size

**TABLE 1** Calculated values of fit parameters  $a_1$  and  $b_1$  (Equation (14)) and  $a_2$  and  $b_2$  (Equation (15));  $\mu$  (i.e.,  $m_1$ ),  $d_{50}$ ,  $d[2, 3]$  and  $d[3, 4]$  given in Table S2

Parameter	Thomas <sup>16,17</sup>	Choice for $d_p$			
		$\mu$ or $m_1$	$d_{50}$	$d[2, 3]$	$d[3, 4]$
$a_1$	10,055	5.43	136	20.2	2,340
$b_1$	−2	2.84	1.36	3.21	−0.362
$a_2$	14	131	124	440	366
$b_2$	−0.5	−1.09	−1.26	−2.59	−1.62

distribution through, for example, the log-normal standard deviation,  $\sigma$ ; and (b) the divergence from ideal, hard-sphere rheological behavior exhibited by a suspension or its tendency to aggregate or flocculate, as measured through a proxy such as, say: (a) its maximum packing fraction relative to that of hard-sphere species with identical size distributions<sup>4,72,73,76</sup>; or (b) its measured viscosity relative to that of an equivalent hard-sphere species.<sup>31,74,75</sup>

## 4 | CONCLUSIONS

A sophisticated in-line rheometric technique was demonstrated in suspensions with low solids loadings. It was shown that the technique, when used on a vertical flow section to eliminate the effects of settling and a solids concentration gradient across the pipe, can be extended to lower solids loadings, viscosities and flow velocities than in previous studies. In such suspensions, in-line rheometry has major advantages over off-line rheometry, as suspensions in the latter can undergo rapid sedimentation, making the measurement of viscosity challenging. This capability of in-line rheometry confers greater safety to operators in many industries. It precludes the need to take physical samples, as well as offering greater assurance that, in the absence of a concentration gradient across the pipe diameter, the measured rheological properties are accurate. The ability of two models to predict the flow properties of complex suspensions—specifically the Fanning friction factor—was assessed with the HB and HBE models. It was found that, of the two models for predicting the friction factor that were tested, that of Madlener et al<sup>41</sup> performed better and is recommended in general on that basis and because it was derived analytically.

The influence of solids volume fraction and particle size on the rheology of complex solid-liquid suspensions was investigated. By combining the in-line method with off-line measurements, it was possible to reassess the dependence of yield stress and relative viscosity on particle size put forward by Thomas<sup>16,17</sup> and it was found that particle size as a single measure was not sufficient to account for the observations. In particular, the yield stress of suspensions was found to increase with particle size, and the effective suspension viscosity to decrease with particle size; a per-species investigation of the influence of particle size on rheology would be a valuable topic in any future study. Agreement with other studies was mixed as there is no clear picture of the mechanisms through which rheology is influenced by particle size and aggregation state. These unanswered questions, central to understanding the rheology of complex suspensions, are left as subjects for future study. However, it is suggested that, as well as mean particle size, the width of the particle size distribution and the divergence from ideal, hard-sphere behavior or tendency to aggregate/flocculate (e.g., via the maximum packing fraction or effective viscosity) must be considered.

## ACKNOWLEDGMENTS

The authors thank the UK Engineering and Physical Sciences Research Council (EPSRC) for financial support of this study through grant EP/L014041/1: Decommissioning, Immobilisation, and Storage Solutions for Nuclear Waste Inventories (DISTINCTIVE). The authors also

thank Peter Dawson, Bob Harris, Tony Windross, Gareth Keevil, and Rob Thomas for their technical assistance, and Olivier Mariette at Met-Flow, Switzerland, for his support and advice. Thanks also go to Prof. Megan Povey for her support in several aspects of the acoustic method, including modeling the speed of sound in suspensions. We also thank the editor and anonymous reviewers for their comments, which improved the article.

## ORCID

Hugh P. Rice  <https://orcid.org/0000-0002-6895-8325>

## REFERENCES

1. NDA. *Radioactive Wastes in the UK: A Summary of the 2016 Inventory*. Cumbria: Nuclear Decommissioning Authority; 2017.
2. Hastings JJ, Rhodes D, Fellerman AS, McKendrick D, Dixon C. New approaches for sludge management in the nuclear industry. *Powder Technol*. 2007;174(1-2):18-24.
3. Paul N, Biggs S, Edmondson M, Hunter TN, Hammond RB. Characterising highly active nuclear waste simulants. *Chem Eng Res des*. 2013;91(4):742-751.
4. Johnson M, Peakall J, Fairweather M, Biggs S, Harbottle D, Hunter TN. Characterization of multiple hindered settling regimes in aggregated mineral suspensions. *Ind Eng Chem Res*. 2016;55(37):9983-9993.
5. Gregson CR, Hastings JJ, Sims HE, Steele HM, Taylor RJ. Characterisation of plutonium species in alkaline liquors sampled from a UK legacy nuclear fuel storage pond. *Anal Methods*. 2011;3(9):1957-1968.
6. Hunter TN, Darlison L, Peakall J, Biggs S. Using a multi-frequency acoustic backscatter system as an in situ high concentration dispersion monitor. *Chem Eng Sci*. 2012;80:409-418.
7. Hunter TN, Peakall J, Biggs S. An acoustic backscatter system for in situ concentration profiling of settling flocculated dispersions. *Miner Eng*. 2012;27:20-27.
8. Hunter TN, Peakall J, Unsworth TJ, et al. The influence of system scale on impinging jet sediment erosion: observed using novel and standard measurement techniques. *Chem Eng Res des*. 2013;91(4):722-734.
9. Rice HP, Fairweather M, Hunter TN, Mahmoud B, Biggs S, Peakall J. Measuring particle concentration in multiphase pipe flow using acoustic backscatter: generalization of the dual-frequency inversion method. *J Acoust Soc Am*. 2014;136(1):156-169.
10. Rice HP, Fairweather M, Peakall J, Hunter TN, Mahmoud B, Biggs SR. Measurement of particle concentration in horizontal, multiphase pipe flow using acoustic methods: limiting concentration and the effect of attenuation. *Chem Eng Sci*. 2015;126:745-758.
11. Bux J, Paul N, Hunter TN, Peakall J, Dodds JM, Biggs S. In situ characterization of mixing and sedimentation dynamics in an impinging jet ballast tank via acoustic backscatter. *AIChE J*. 2017;63(7):2618-2629.
12. Rice HP, Fairweather M, Peakall J, Hunter TN, Mahmoud B, Biggs SR. Constraints on the functional form of the critical deposition velocity in solid-liquid pipe flow at low solid volume fractions. *Chem Eng Sci*. 2015;126:759-770.
13. Rice HP, Fairweather M, Hunter TN, Peakall J, Biggs SR. The influence of relative fluid depth on initial bedform dynamics in closed, horizontal pipe flow. *Int J Multiphas Flow*. 2017;93:1-16.
14. Talbot A. High shear viscometry of concentrated solutions of poly (alkylmethacrylate) in a petroleum lubricating oil. *Rheol Acta*. 1974;13(2):305-317.
15. Duda JL, Klaus EE, Lin SC. Capillary viscometry study of non-Newtonian fluids—influence of viscous heating. *Ind Eng Chem Res*. 1988;27(2):352-361.

16. Thomas DG. Transport characteristics of suspensions—part III. Laminar-flow properties of flocculated suspensions. *AIChE J.* 1961;7(3):431-437.
17. Thomas DG. Non-Newtonian suspensions—part I. Physical properties and laminar transport characteristics. *Ind Eng Chem.* 1963;55(11):18-29.
18. White SA, Gotsis AD, Baird DG. Review of the entry flow problem—experimental and numerical. *J Non-Newtonian Fluid Mech.* 1987;24(2):121-160.
19. Kamal MR, Nyun H. Capillary viscometry: a complete analysis including pressure and viscous heating effects. *Polym Eng Sci.* 1980;20(2):109-119.
20. Mooney M. Explicit formulas for slip and fluidity. *J Rheol.* 1931;2(2):210-222.
21. Rabinowitsch B. Viscosity and elasticity of sols. *Z Phys Chem.* 1929;145(1):1-26.
22. Wiklund J, Stading M, Tragardh C. Monitoring liquid displacement of model and industrial fluids in pipes by in-line ultrasonic rheometry. *J Food Eng.* 2010;99(3):330-337.
23. Wassell P, Wiklund J, Stading M, et al. Ultrasound Doppler based in-line viscosity and solid fat profile measurement of fat blends. *Int J Food Sci Technol.* 2010;45(5):877-883.
24. Kotzé R, Haldenwang R, Fester V, Rössle W. In-line rheological characterisation of wastewater sludges using non-invasive ultrasound sensor technology. *Water SA.* 2015;41(5):683-690.
25. Machin TD, Wei H-Y, Greenwood RW, Simmons MJH. In-pipe rheology and mixing characterisation using electrical resistance sensing. *Chem Eng Sci.* 2018;187:327-341.
26. Ouriev B, Windhab E. Rheological study of concentrated suspensions in pressure-driven shear flow using a novel in-line ultrasound Doppler method. *Exp Fluids.* 2002;32(2):204-211.
27. Johnson M, Fairweather M, Harbottle D, Hunter TN, Peakall J, Biggs S. Yield stress dependency on the evolution of bubble populations generated in consolidated soft sediments. *AIChE J.* 2017;63(9):3728-3742.
28. Bux J, Peakall J, Rice HP, Manga MS, Biggs S, Hunter TN. Measurement and density normalisation of acoustic attenuation and backscattering constants of arbitrary suspensions within the Rayleigh scattering regime. *ApAc.* 2019;146:9-22.
29. Elliott LN, Bourne RA, Hassanpour A, Edwards JL, Sutcliffe S, Hunter TN. Salt enhanced solvent relaxation and particle surface area determination via rapid spin-lattice NMR. *Powder Technol.* 2018;333:458-467.
30. Allen T. *Particle Size Measurement.* 3rd ed. London and New York: Chapman and Hall; 1981.
31. Mwasame PM, Wagner NJ, Beris AN. Modeling the effects of polydispersity on the viscosity of noncolloidal hard sphere suspensions. *J Rheol.* 2016;60(2):225-240.
32. Balastre M, Argillier JF, Allain C, Foissy A. Role of polyelectrolyte dispersant in the settling behaviour of barium sulphate suspension. *Colloids Surf A.* 2002;211(2):145-156.
33. Balastre M, Persello J, Foissy A, Argillier JF. Binding and ion-exchange analysis in the process of adsorption of anionic polyelectrolytes on barium sulfate. *J Colloid Interface Sci.* 1999;219(1):155-162.
34. Met-Flow. *UVP Monitor Model UVP-Duo with Software Version 3.* Lausanne, Switzerland: Met-Flow SA; 2002.
35. Takeda Y. Velocity profile measurement by ultrasonic Doppler method. *Exp Therm Fluid Sci.* 1995;10(4):444-453.
36. Wiklund JA, Stading M, Pettersson AJ, Rasmuson A. A comparative study of UVP and LDA techniques for pulp suspensions in pipe flow. *AIChE J.* 2006;52(2):484-495.
37. Wunderlich T, Brunn PO. Ultrasound pulse Doppler method as a viscometer for process monitoring. *Flow Meas Instrum.* 1999;10(4):201-205.
38. Peker SM, Helvacı SS. *Solid-liquid two phase flow.* Amsterdam: Elsevier; 2007.
39. Benslimane A, Bekkour K, Francois P, Bechir H. Laminar and turbulent pipe flow of bentonite suspensions. *J Petrol Sci Eng.* 2016;139:85-93.
40. Chilton RA, Stainsby R. Pressure loss equations for laminar and turbulent non-Newtonian pipe flow. *J Hydraul Eng-ASCE.* 1998;124(5):522-529.
41. Madlener K, Frey B, Ciezki H. Generalized Reynolds number for non-Newtonian fluids. In: BC DLL, Haidn O, Frolov S, eds. *Progress in propulsion physics.* Vol 1. Les Ulis, France: EDP Sciences; 2009:237-250.
42. Wiklund J, Stading M. Application of in-line ultrasound Doppler-based UVP-PD rheometry method to concentrated model and industrial suspensions. *Flow Meas Instrum.* 2008;19(3-4):171-179.
43. Madlener K, Ciezki H. Theoretical investigation of the flow behavior of gelled fuels of the extended Herschel–Bulkley type. *36th Conference (International) of ICT & 32nd Pyrotechnics Seminar (International).* Karlsruhe; 2005.
44. Madlener K, Ciezki H. Analytical description of the flow behavior of extended Herschel–Bulkley fluids with regard to gel propellants. *1st European Conference for Aerospace Sciences (EUCASS2005).* Moscow, Germany: Fraunhofer Institute for Chemical Technology; 2005.
45. Markis F, Baudez JC, Parthasarathy R, Slatter P, Eshtiaghi N. Rheological characterisation of primary and secondary sludge: impact of solids concentration. *Chem Eng J.* 2014;253:526-537.
46. Dabak T, Yucel O. Modeling of the concentration and particle size distribution effects on the rheology of highly concentrated suspensions. *Powder Technol.* 1987;52(3):193-206.
47. Smith TL, Bruce CA. Intrinsic viscosities and other rheological properties of flocculated suspensions of nonmagnetic and magnetic ferric oxides. *J Colloid Interface Sci.* 1979;72(1):13-26.
48. Heywood NI, Richardson JF. Rheological behaviour of flocculated and dispersed aqueous kaolin suspensions in pipe flow. *J Rheol.* 1978;22(6):599-613.
49. Gillespie T. The effect of aggregation and particle size distribution on the viscosity of Newtonian suspensions. *J Colloid Interface Sci.* 1983;94(1):166-173.
50. Kotzé R, Haldenwang R, Fester V, Rössle W. A feasibility study of in-line rheological characterisation of a wastewater sludge using ultrasound technology. *Water SA.* 2014;40(4):579-585.
51. Pfund DM, Greenwood MS, Bamberger JA, Pappas RA. Inline ultrasonic rheometry by pulsed Doppler. *Ultra.* 2006;44:E477-E482.
52. Roberson JA, Crowe CT. *Engineering fluid mechanics.* New York, NY: John Wiley & Sons; 1996.
53. Koseli V, Zeybek S, Uludag Y. Online viscosity measurement of complex solutions using ultrasound Doppler velocimetry. *Turk J Chem.* 2006;30(3):297-305.
54. Dogan N, McCarthy MJ, Powell RL. Measurement of polymer melt rheology using ultrasonics-based in-line rheometry. *Meas Sci Technol.* 2005;16(8):1684-1690.
55. Bird RB, Armstrong RC, Hassager O. *Dynamics of polymeric liquids.* 2nd ed. New York, NY: Wiley; 1987.
56. Metzner AB, Reed JC. Flow of non-Newtonian fluids—correlation of the laminar, transition, and turbulent-flow regions. *AIChE J.* 1955;1(4):434-440.
57. Govier GW, Aziz K. *The flow of complex mixtures in pipes.* Vol 469. New York, NY: Van Nostrand Reinhold; 1972.
58. Zhou ZW, Solomon MJ, Scales PJ, Boger DV. The yield stress of concentrated flocculated suspensions of size distributed particles. *J Rheol.* 1999;43(3):651-671.
59. Banfill PFG. Rheological methods for assessing the flow properties of mortar and related materials. *Construct Build Mater.* 1994;8(1):43-50.
60. Van den Tempel M. Rheology of concentrated suspensions. *J Colloid Interface Sci.* 1979;71(1):18-20.

61. Buscall R, Mills P, Stewart R, Sutton D, White L, Yates G. The rheology of strongly-flocculated suspensions. *J Non-Newtonian Fluid Mech.* 1987;24(2):183-202.
62. Tanaka H, White JL. A cell model theory of the shear viscosity of a concentrated suspension of interacting spheres in a non-Newtonian fluid. *J Non-Newtonian Fluid Mech.* 1980;7(4):333-343.
63. Michaels AS, Bolger JC. The plastic flow behavior of flocculated kaolin suspensions. *Ind Eng Chem Fundam.* 1962;1(3):153-162.
64. Hunter RJ, Nicol S. The dependence of plastic flow behavior of clay suspensions on surface properties. *J Colloid Interface Sci.* 1968;28(2):250-259.
65. Firth BA, Hunter RJ. Flow properties of coagulated colloidal suspensions: III. The elastic floc model. *J Colloid Interface Sci.* 1976;57(2):266-275.
66. Doi M, Chen D. Simulation of aggregating colloids in shear flow. *J Chem Phys.* 1989;90(10):5271-5279.
67. Chen D, Doi M. Simulation of aggregating colloids in shear flow II. *J Chem Phys.* 1989;91(4):2656-2663.
68. Viamajala S, McMillan JD, Schell DJ, Elander RT. Rheology of corn Stover slurries at high solids concentrations-effects of saccharification and particle size. *Bioresour Technol.* 2009;100(2):925-934.
69. Ancy C, Jorrot H. Yield stress for particle suspensions within a clay dispersion. *J Rheol.* 2001;45(2):297-319.
70. Singh MK, Ratha D, Kumar S, Kumar D. Influence of particle-size distribution and temperature on rheological behavior of coal slurry. *Int J Coal Prep Util.* 2016;36(1):44-54.
71. Li CX, Zhou ZY, Zou RP, Dong KJ, Pinson D, Yu AB. Equivalent packing size of spheroidal particles: a microscopic test. *Powder Technol.* 2018;333:286-292.
72. Hao T, Riman RE. Methodology for determination of the maximum packing fraction for particle-filled polymer suspensions. *Particul Sci Technol.* 2003;21(4):317-325.
73. Ouchiyama N, Tanaka T. Porosity of a mass of solid particles having a range of sizes. *Ind Eng Chem Fundam.* 1981;20(1):66-71.
74. Mwasame PM, Wagner NJ, Beris AN. Modeling the viscosity of poly-disperse suspensions: improvements in prediction of limiting behavior. *Phys Fluids.* 2016;28(6):061701.
75. Mendoza CI, Santamaria-Holek I. The rheology of hard sphere suspensions at arbitrary volume fractions: an improved differential viscosity model. *J Chem Phys.* 2009;130(4):044904.
76. Rice Hugh P., Peakall Jeffrey, Fairweather Michael, Hunter Timothy N. Extending estimation of the critical deposition velocity in solid-liquid pipe flow to ideal and non-ideal particles at low and intermediate solid volume fractions. *Chemical Engineering Science.* 2020;211:115308. <http://dx.doi.org/10.1016/j.ces.2019.115308>.

### SUPPORTING INFORMATION

Additional supporting information may be found online in the Supporting Information section at the end of this article.

**How to cite this article:** Rice HP, Pilgrim JL, Fairweather M, Peakall J, Harbottle D, Hunter TN. Extending acoustic in-line pipe rheometry and friction factor modeling to low-Reynolds-number, non-Newtonian slurries. *AIChE Journal.* 2020;66:e16268. <https://doi.org/10.1002/aic.16268>